Inorganic Chemistry

Article

pubs.acs.org/IC

Stabilizing Coordinated Radicals via Metal–Ligand Covalency: A Structural, Spectroscopic, and Theoretical Investigation of Group 9 Tris(dithiolene) Complexes

Thorbjørn J. Morsing,[†,‡] Samantha N. MacMillan,[†] Jacob W. H. Uebler,[†] Theis Brock-Nannestad,[‡] Jesper Bendix,[‡] and Kyle M. Lancaster*[,†]

[†]Department of Chemistry and Chemical Biology, Baker Laboratory, Cornell University, Ithaca, New York 14853, United States

[‡]Department of Chemistry, University of Copenhagen, Universitetsparken 5, 2100 Copenhagen, Denmark

Supporting Information

ABSTRACT: Proper assignment of redox loci in coordination complexes with redox-active ligands to either the metal or the ligand is essential for rationalization of their chemical reactivity. However, the high covalency endemic to complexes of late, third-row transition metals complicates such assignments. Herein, we systematically explore the redox behavior of a series of group 9 tris(dithiolene) complexes, $[M(mnt)_3]^{3-}$ (M = Ir, Rh, Co; mnt = maleonitriledithiolate). The Ir species described comprise the first examples of homoleptic Ir dithiolene complexes. The enhanced metal–ligand covalency of the Ir–S interaction leads to remarkable reactivity of $[Ir(mnt)_3]^{3-}$ and stabilization of mononuclear $[Ir(mnt)_3]^{2-}$ complex ions as well as dimerized versions featuring weak, covalent, intermolecular S–S bonds. The dianionic Rh and Co analogues are, in contrast, highly unstable, resulting in the rapid formation of $[Rh_2(mnt)_5]^{4-}$ and $[Co(mnt)_2]_2^{2-}$, respectively. The synthesized complexes were studied by single-crystal X-ray diffraction, X-ray absorption spectroscopy, optical spectroscopy, magnetometry, density functional theory, and spectroscopy-oriented configuration interaction calculations. Spectroscopic and theoretical analyses suggest that the stability of $[Ir(mnt)_3]^{2-}$ may be attributed to dilution of ligand radical character by a high degree of Ir 5d character in the singly occupied molecular orbital.

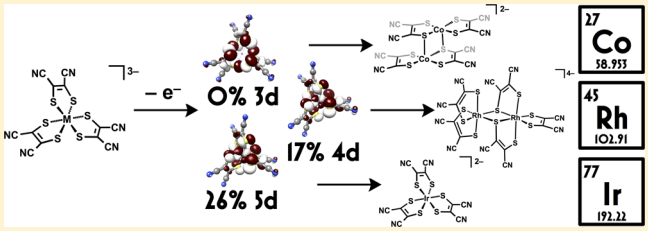

INTRODUCTION

Since the 1960s, the chemistry of metal dithiolene complexes has fascinated chemists, sparking heated debates about their electronic structures and spurring the development and application of new bonding models and spectroscopic methods.[1−3] Indeed, these early examples of "redox noninnocence" have birthed an entire field of study related to complexes of redox noninnocent ligands and their use in energy conversion, materials applications, and catalysis.[4−8] Fundamental electronic structure studies, particularly those employing high-resolution X-ray crystallography, X-ray absorption spectroscopy (XAS), density functional theory (DFT), and ab initio calculations have enabled systematic distinction between formal and physical oxidation states in these types of complexes.[9−12] This bifurcation of redox loci has facilitated evaluation and tuning of the relative roles of ligand-centered and metal-centered redox on chemical reactivity.[13−16]

Intrinsically larger metal–ligand covalencies complicate systematic understanding of the redox behavior of late, 5d complexes with redox-active ligands. For example, a recent comparison of complexes of the redox-active tris(pentafluorophenyl)corrole (tpfc) ligand with group 9 metals demonstrated that "ligand-centered" and "metal-centered" labels for redox events are inappropriate for the Ir congener.[17] Rather, one-electron oxidation of $(tpfc)Ir(py)_2$ (py = pyridine) is better described as "molecular redox," where the radical is equally distributed over the entire molecule. Conversely, radicals in the Rh and Co congeners completely lack metal character. This behavior was attributed to enhanced metal–ligand orbital overlap due to the radial expansion of the 5d orbitals in Ir arising as a consequence of relativistic core orbital contraction.[18−21]

To further explore molecular redox behavior and its potential consequences on chemical reactivity, a series of group 9 tris(mnt) (mnt = maleonitriledithiolate) complexes was synthesized. Although $[Co(mnt)_3]^{3-}$ is a stable species that has been known for some time, the one-electron oxidized $[Co(mnt)_3]^{2-}$ has never been isolated.[22] This instability was presumed, based on electrochemical measurements, to be due to ligand dissociation. Given that the Ir congener will exhibit greater M–S covalency, $[Ir(mnt)_3]^{2-}$ should be stable to isolation and characterization.

EXPERIMENTAL SECTION

Syntheses. *General Considerations.* All reactions were performed under an atmosphere of N_2 using fully dried and degassed solvents unless otherwise noted. Acetonitrile (BDH Chemicals) was dried by

Received: February 5, 2015
Published: March 10, 2015

ACS Publications © 2015 American Chemical Society

DOI: 10.1021/acs.inorgchem.5b00289
Inorg. Chem. 2015, 54, 3660−3669

the method of Grubbs using a JC Meyer Solvent System. *N*,*N*-Dimethylformamide (DMF, Mallinckrodt) was dried over 4 Å molecular sieves. Ethyl acetate (Fisher) and methanol (Macron) for chromatography were used as received. Hydrated $IrCl_3$ was purchased from Pressure Chemical and used as received. (ASN)Br (ASN = 5-azonia-spiro[4,4]nonane)[23] and Na_2mnt[24] were synthesized according to published procedures and dried under high (≤5 mTorr) vacuum before use.

$(ASN)_3[Ir(mnt)_3]$ ($1[ASN]_3$). 300 mg (0.85 mmol) of $IrCl_3{\cdot}3H_2O$ was refluxed with stirring under N_2 for 24 h in 50 mL of dry CH_3CN in a 125 mL flask to afford a clear yellow solution of $IrCl_3(NCCH_3)_3$. This solution was taken to dryness on a rotary evaporator. The flask was then charged with 570 mg (3.1 mmol) of Na_2mnt and 30 mL of dry DMF. This mixture was degassed via three freeze−pump−thaw cycles and subsequently heated to reflux for 24 h under N_2. The obtained dark red solution was evaporated to dryness on a high vacuum line to yield a dark oily residue that was subsequently dissolved in 6 mL of a 1:1 ethyl acetate/methanol mixture. This solution was loaded onto a 5 cm alumina column equilibrated with ethyl acetate. The column was washed with two volumes of ethyl acetate to remove trace DMF, and the product was subsequently eluted with neat methanol. The eluent solution containing the product (presumably $Na_3[Ir(mnt)_3]$) was evaporated to dryness. This material was dissolved in 4 mL of methanol and filtered. A solution of 1.1 g of (ASN)Br (5.3 mmol) in 1.5 mL of methanol was added quickly, immediately yielding a turbid solution. All precipitate giving rise to this turbidity subsequently dissolved within seconds and then reprecipitated over the course of 5 min. The now-persistent precipitate was pelleted by centrifugation, the supernatant was decanted, and the precipitate was triturated with 3 × 5 mL of ethanol. The red product was then transferred to a flask containing 50 mL of 2-propanol and 70 mL of acetone. Upon standing, orange-red crystals formed that were subsequently collected on a fritted glass funnel, washed with ethanol, and dried under vacuum. Yield: 288 mg (32% based on $IrCl_3{\cdot}3H_2O$) ^{13}C NMR (125.7 MHz, CD_3CN): δ: 120.26, 125.69. IR: See Supporting Information, Table S1. UV−vis, cm^{-1} (ε, M^{-1} cm^{-1}): 21 900 (6780), 24 450 (6460), 29 400 (12 200), 33 100 (19 100), 38 200 (15 000). Electrospray ionization mass spectrometry (ESI-MS): See Supporting Information, Table S2. Anal. Calcd for $C_{36}H_{48}N_9S_6Ir$: C, 43.61; H, 4.88; N, 12.71. Found: C, 43.28; H, 4.66; N, 12.56.

$(PPh_4)_3[Ir(mnt)_3]$ ($1[PPh_4]_3$). The procedure for the synthesis of $1[ASN]_3$ was followed, starting from 0.333 g of $IrCl_3{\cdot}3H_2O$ (1 mmol), until the addition of (ASN)Br. Instead 2.2 g (5.87 mmol) of $(Ph_4P)Cl$ was dissolved in 2 mL of methanol and added to the methanol solution of $Na_3[Ir(mnt)_3]$. A dark red oil immediately precipitated, and the supernatant was decanted off. The oil was thoroughly washed with methanol and dried under a stream of N_2. Diethyl ether was added, and the solid product precipitated. It was washed 4−5 times with copious amounts of diethyl ether and dried in air. Yield: 0.82 g (53.3). Elemental Anal. Calcd: C: 61.88, H: 3.17, N: 5.15. Found: C: 61.42, H: 3.01, N: 5.36.

$(ASN)_3[Rh(mnt)_3]$ ($2[ASN]_3$). This molecule was synthesized following a similar method as for $1[ASN]_3$, using 325 mg (1.23 mmol) of $RhCl_3{\cdot}3H_2O$ and 690 mg (3.71 mmol) of Na_2mnt. Yield: 475 mg (43%) of a deep red crystalline solid. ^{13}C NMR (125.7 MHz, CD_3CN): δ: 119.69/119.70 (J_{Rh} =1.9 Hz), 126.48. IR: See Table S1. UV−vis, cm^{-1} (ε, M^{-1} cm^{-1}): 23 100 (13 000), 32 200 (22 200), 35 800 (44 700), 40 000 (113 400), 45 700 (81 600). ESI-MS: See Table S2. Anal. Calcd for $C_{36}H_{48}N_9S_6Rh$: C, 47.93; H, 5.36; N, 13.97. Found: C, 47.75; H, 5.24; N, 13.83.

$(ASN)_3[Co(mnt)_3]$ ($3[ASN]_3$). Synthesized by adaptation of a literature procedure:[22] 0.75 g (4.03 mmol) of Na_2mnt and 0.35 g (1.19 mmol) of $Na_3[Co(CO_3)_3]{\cdot}3H_2O$ were refluxed in 110 mL of ethanol for 2 h. The dark green solution was filtered hot into an ice-cold solution of 1.1 g (5.3 mmol) of (ASN)Br in 50 mL of ethanol and left for half an hour to precipitate. The crude solid was filtered, dissolved in acetone, and filtered again. 2-Propanol was added to the filtrate. The resulting solution was allowed to evaporate for 36 h, affording dark green needles that were collected by filtration, washed with ethanol, and dried in vacuo. Yield: 232 mg (28%) ^{13}C NMR (125.7 MHz, CD_3CN): δ: 118.90, 126.88. IR: See Table S1. UV−vis, cm^{-1} (ε, M^{-1} cm^{-1}): 15 400 (1200), 22 500 (5450), 34 400 (40 000), 43 500 (24 800). ESI-MS: See Table S2. Anal. Calcd for $C_{36}H_{48}N_9S_6Co$: C, 50.39; H, 5.64; N, 14.70. Found: C, 50.09; H, 5.50; N, 14.86.

$\{(ASN)_2[Ir(mnt)_3]\}_2{\cdot}CH_2Cl_2$ ($\{4[ASN]_2\}_2$). 93 mg (0.094 mmol) of $1[ASN]_3$ and 26 mg (0.079 mmol) of $FcPF_6$ were suspended in 100 mL of dichloromethane and stirred vigorously for 5 min, during which time the solution turned dark green. The solution was filtered to remove excess $1[ASN]_3$, and diethyl ether was vapor diffused into it over 48 h. The product was removed by filtration, washed with diethyl ether, and dried. Yield: 72 mg (quantitative with respect to Fc^+). IR: See Table S1. UV−vis, cm^{-1} (ε, M^{-1} cm^{-1}): 15 600 (1500), 26 200 (9200), 28 500 (8200), 34 500 (18 900), 38 000 (23 500). ESI-MS: See Table S2. Anal. Calcd for $C_{28.5}H_{33}ClN_8S_6Ir$: C, 37.74; H, 3.67; N, 12.35. Found: C, 38.11; H, 3.35; N, 12.31.

$(PPh_4)_2[Ir(mnt)_3]$ ($4[PPh_4]_2$). 200 mg (0.122 mmol) of $1[PPh_4]_3$ and 41 mg (0.124 mmol) of $FcPF_6$ were placed in a flask and dissolved in 10 mL of dichloromethane. After standing for an hour, the solution was filtered, and diethyl ether was vapor diffused into it. Precipitation of colorless $(Ph_4P)PF_6$ began almost immediately (identity confirmed by single-crystal analysis), and when the green product started to precipitate, the solution was filtered to remove $(Ph_4P)PF_6$, and the ether diffusion continued until the solution was only slightly colored. The product was removed by filtration and washed with diethyl ether. Yield: 92 mg (58%). This initial product is not completely pure as shown by elemental analysis: Anal. Calcd C: 55.82, H: 3.12, N: 6.51. Found. 56.66, H: 2.90, N: 6.48. Small portions used for further studies were purified by dissolving in dichloromethane and then dropwise addition of ether, producing a fine needlelike precipitate: Found. 55.93, H: 2.96, N: 6.52.

$(ASN)_4[Rh_2(mnt)_5]{\cdot}CH_3CH(OH)CH_3$ ($5[ASN]_4$). 85 mg (0.094 mmol) of $2[ASN]_3$ and 26 mg (0.079 mmol) of $FcPF_6$ were suspended in 50 mL of 2-propanol. Acetone was added until all solid dissolved, giving a maroon solution. This solution was filtered and then concentrated in air giving a dark brown (almost black) precipitate that was filtered and dried. Yield: 26 mg (45%). IR: See Table S1. UV−vis, cm^{-1} (ε, M^{-1} cm^{-1}): 23 300 (8700), 32 200 (18 000), 37 500 (33 500), 41 000 (42 600). ESI-MS: See Table S2. Anal. Calcd for $C_{55}H_{72}N_{14}OS_{10}Rh_2$: C, 44.92; H, 4.93; N, 13.33. Found: C, 44.78; H, 4.57; N, 13.53.

$(ASN)_2[Co_2(mnt)_4]$ ($\{6[ASN]\}_2$). 232 mg (0.270 mmol) of $3[ASN]_3$ and 75 mg (0.227 mmol) of $FcPF_6$ were suspended in 50 mL of 2-propanol. 100 mL of acetone was added to fully dissolve both compounds. The resulting dark brown solution was filtered and left to evaporate for 18 h. Brown, needlelike crystals of product were filtered off, washed with ethanol, and air-dried. Yield: 81 mg (77%). IR: See Table S1. UV−vis, cm^{-1} (ε, M^{-1} cm^{-1}): 12 500 (3200), 18 200 (2600), 21 800 (4700), 24 100 (5700), 27 100 (7400), 32 700 (21 000), 37 500 (26 900). MS (ESI): See Table S2. Anal. Calcd for $C_{32}H_{32}N_{10}S_8Co_2$: C, 41.32; H, 3.47; N, 15.05. Found: C, 41.54; H, 3.22; N, 14.99.

$(PPh_4)_2(mnt_2)_2$, Tetraphenylphosphonium (*Z*)-2-[(*Z*)-1,2-dicyano-2-thioxoethenyldithio]-3-thioxo-2-butenedinitrile. The addition of tetraphenylphosphonium to a solution of sodium maleonitriledithiolene effects the oxidation of mnt^{2-} by air to give $(mnt_2)^{2-}$ as the Ph_4P salt: 1 g (5.3 mmol) of Na_2mnt was dissolved in 10 mL of water, and 0.330 g (0.88 mmol) of $(PPh_4)Cl$ was dissolved in 25 mL of water. Both solutions were filtered and then poured together. An orange precipitate formed immediately. The solid was removed by filtration, washed with copious amounts of water, and air-dried. The yield is quantitative with regard to $(PPh_4)Cl$, but the compound is not completely pure as gauged by the mass of the product, which slightly exceeds the expected 0.43 g. Small amounts of the crude product (50 mg portions) were recrystallized from acetonitrile (with 1% water added) by diffusion of ^{t}BuOMe into this solution. This method afforded crystals suitable for X-ray crystallography. UV−vis, cm^{-1} (ε, M^{-1} cm^{-1}): 22 700 (16 700), 26 500 (17 500), 43 300 (14 800). ESI-MS, m/z: 139.9505 (mnt^-).

DOI: 10.1021/acs.inorgchem.5b00289
Inorg. Chem. 2015, 54, 3660−3669

PHYSICAL METHODS

X-ray Crystallography and Refinement of Structures. Single-crystal X-ray diffraction studies were performed using a Siemens P4 SMART CCD area detector with a graphite-monochromated Mo Kα (λ = 0.710 73 Å) radiation source for the structure of $\{\mathbf{6}[\mathbf{ASN}]\}_2$. For the rest of the structures, the data were collected on a Bruker D8 Venture diffractometer monochromated with a doubly curved silicon crystal (also Mo Kα). The data sets were collected and processed using Bruker Apex 2 with the SAINT[25] and SADABS[26] programs and refined using Olex2.[27] All hydrogen atoms were added using a riding model and refined with an isotropic displacement factor of 1.2U_{eq} of the parent atom.

X-ray Absorption Spectroscopy. Ir L_3- and L_1-edge XAS spectra were measured at the Stanford Synchrotron Radiation Lightsource (SSRL) beamline 9−3 under ring conditions of 3 GeV and 500 mA. A Si(220) double-crystal monochromator was used for energy selection. A Rh-coated mirror (set to an energy cutoff of 15 keV) was used for harmonic rejection. Internal energy calibration was performed for each individual spectrum by assigning the first inflection points of the spectrum of a finely dispersed $K_2[IrCl_6]$ on Kapton to 13 419 eV (Ir L_1). Data were collected in transmission mode on finely ground samples of the dithiolene complexes diluted in BN pressed into 1 mm Al spacers sealed with 38 μm Kapton tape. Sample temperatures were maintained at 10 K in an Oxford liquid He flow cryostat. L_1-edge data were collected from 13 180 to 13 740 eV; L_3-edge data were collected from 10 985 to 12 115 eV to measure extended X-ray absorption fine structure (EXAFS) to k = 15 Å^{-1}. Two L_3 and four L_1 scans were averaged and processed using the SIXPACK software package.[28] Background subtraction was achieved by fitting a polynomial to the pre-edge region and subtracting this polynomial from the entire spectrum. Spectra were normalized by fitting a flattened polynomial to the postedge (L_1-edge: 13 425; L_3-edge: 11 235) and normalizing the edge jump to 1.0. EXAFS data were fit using the OPT package of EXAFSPAK using paths calculated using FEFF7.[29,30]

The S K-edge XAS spectra were measured at SSRL beamline 4−3 under ring conditions of 3 GeV and 500 mA. Samples were prepared by grinding to a fine powder and were spread to a vanishing thickness onto 38 μm low-S Mylar tape. All samples were measured in a He atmosphere at room temperature in fluorescence mode using a Lytle detector. The incident beam energy was calibrated by setting the energy of the first peak in the S K-edge spectrum of $Na_2S_2O_3{\cdot}5H_2O$ to 2472.02 eV. Intensity was normalized with respect to the incident beam using a He-filled ion chamber upstream of the sample. Data represent an average of four scans measured from 2420 to 2720 eV. Data were processed with SIXPACK in a manner similar to those of the Ir XAS. Spectra were normalized by fitting a polynomial flattened to energies below 2490 eV to the data and normalizing the region below 2490 eV to unity.

Other Physical Methods. NMR experiments were performed on a Bruker 500 MHz spectrometer equipped with a cryoprobe and operating at 125.7 MHz for ^{13}C measurements. ^{13}C NMR spectra are reported in ppm relative to tetramethylsilane (δ = 0) and were referenced internally to CH_3CN (δ = 118.26). Apart from the shifts given, all measured samples showed the expected signals from the ASN counterions: ^{13}C NMR: singlet at 22.74, triplet at 63.85 (J_N = 3.1 Hz), ^{1}H NMR: multiplets at 2.20 (Int. 1.0) and 3.50 (Int. 1.0). Except for solvent signals, no impurities were observed in any of the recorded spectra. IR spectra were recorded on an Agilent Cary 630 FTIR spectrophotometer. Measurements were taken of pure, powdered samples. Magnetic susceptibility measurements were conducted on an MPMS-XL Quantum-Design SQUID magnetometer on a finely ground sample. The susceptibilities were corrected for diamagnetic contributions from the sample holder and from the sample by means of Pascal's constants, in the temperature range of 2−300 K. The sample was mounted in a diamagnetic capsule, and the measurements were done at 1000 and 3000 Oe.

Standard UV−vis spectra (200−1100 nm) were collected using a Varian Cary 60 scanning spectrophotometer. UV−vis−NIR spectra (NIR = near-infrared; 200−2780 nm) were collected using a Cary 5 scanning spectrophotometer. Spectra for solid samples were measured in transmission mode on finely ground samples pressed between sapphire plates. All voltammetric measurements were performed using a Pine Instruments WaveNow USB Potentiostat/Galvanostat. Compounds were dissolved at ∼1 mM concentration in MeCN containing 0.1 M $(N^nBu_4)PF_6$ as the supporting electrolyte. For cyclic and differential pulse voltammetry, a 3 mm Pt disk working electrode, coiled Pt wire counter electrode, and a single-junction Ag/AgCl reference electrode were employed. Reduction potentials are reported relative to the ferrocenium/ferrocene couple, which was measured as an internal standard following completion of experiments with dithiolene complex analytes. For spectroelectrochemical measurements, a gold "honeycomb" spectroelectrochemical card, which contains a Au working electrode mesh and two Au counter electrode areas, were used, along with a separate single-junction Ag/AgCl reference electrode. Spectra were measured using a Cary 60 UV−vis spectrophotometer. Mass spectra were collected on a Bruker Solarix ESI/MALDI FT-ICR mass spectrometer equipped with a 7 T magnet. The ESI samples were prepared in acetonitrile and measured using external calibration with either L-histidine or sodium trifluoroacetate cluster ions. Data collected were processed in Bruker Dataanalysis 4.0 SP5.

CALCULATIONS

Methods. All calculations were performed using version 2.9.0 of the ORCA quantum chemistry suite.[31] Geometry optimizations were performed for $[M(mnt)_3]^{n-}$ (n = 1, 2, 3) using density functional theory (DFT) with the BP86 exchange correlation functional[32,33] along with the segmented all-electron relativistically contracted (SARC) def2-TZVP(-f) basis set for all atoms.[34,35] Optimizations also included the zeroth order regular approximation (ZORA)[36,37] for relativistic effects and solvation as modeled by the conductor-like screening model (COSMO)[38] using an infinite dielectricum. Integration accuracies were set to Grid7 for transition metal atoms and to Grid4 for ligand atoms. Numerical frequency calculations were performed at the converged geometries to confirm global geometric minima.

The B3LYP hybrid exchange correlation functional,[39] in conjunction with the ZORA-optimized SARC def2-TZVP(-f) basis set on all atoms, was used to generate single-point unrestricted Kohn−Sham (UKS) electronic structure solutions for use in calculation of spectroscopic observables. Electron paramagnetic resonance (EPR) properties were predicted using coupled perturbation Kohn−Sham theory for the g-matrix, and the spin−orbit coupling (SOC) operator was treated by the

DOI: 10.1021/acs.inorgchem.5b00289
Inorg. Chem. 2015, 54, 3660−3669

spin−orbit mean field approximation.[40,41] Electronic absorption spectra were calculated using time-dependent DFT (TDDFT).

Spectroscopy-oriented configuration interaction (SORCI) calculations[42] on crystallographically determined $\{\mathbf{4}[ASN]_2\}_2$ and mnt_2^{2-} were performed to estimate the relative energy separations between the ground and first triplet excited states. SORCI was performed on a complete active space (CAS) for $\{\mathbf{4}[ASN]_2\}_2$ comprising 10 electrons and 6 orbitals (CAS-(10,6)). CAS(10,9) was chosen for mnt_2^{2-}. Active spaces were chosen to include orbitals with S−S bonding and antibonding character. The def2-SV(P) basis set was used for all atoms. As described elsewhere, individual selection was used to ease the computational burden.[42] The size of the first-order interacting space was reduced with a threshold $T_{sel} = 1 \times 10^{-6}$ Eh. A further approximation involves reduction of the reference space through another selection—all initial references that contribute less than a second threshold ($T_{pre} = 1 \times 10^{-5}$) to the zeroth-order states are rejected from the reference space. The initial orbitals for the first step of the SORCI procedure were taken from restricted Kohn−Sham orbitals from a B3LYP/def2-SV(P)/ZORA calculation. We note that the def2-SV(P) basis set was chosen to attenuate the substantial computational expense of ab initio calculation of the $\{\mathbf{4}[ASN]_2\}_2$ electronic structure, and we stress that the values for the bond energies must be taken as qualitative estimates of the relative S−S bond strengths.

RESULTS AND DISCUSSION

Synthesis of $[M(mnt)_3]^{3-}$ (M = Ir, Rh, Co). Prior to this work, no published examples existed of *any* homoleptic Ir dithiolene complexes despite more than half a century of rich dithiolene chemistry.[1−3,9,43,44] Treatment of $IrCl_3(MeCN)_3$ with 3 equiv of Na_2mnt in refluxing DMF affords a red solution, putatively of $Na_3[Ir(mnt)_3]$. After removal of DMF, the complex trianion $(ASN)_3[Ir(mnt)_3]$ ($\mathbf{1}[ASN]_3$) is precipitated as an air-stable, red solid from methanol by the addition of 5-azonia-spiro[4,4]nonane bromide ((ASN)Br, Scheme 1, 32% yield). Starting from $RhCl_3(MeCN)_3$, the Rh

Scheme 1. Synthesis of $[M(mnt)_3]^{3-}$ (M = Ir, Rh, Co) Salts

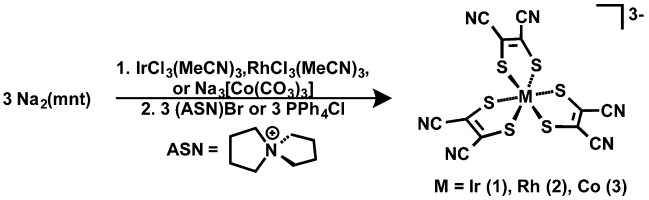

congener, $(ASN)_3[Rh(mnt)_3]$ ($\mathbf{2}[ASN]_3$), is isolated in 43% yield, following the same procedure. The synthesis of $[Co(mnt)_3]^{3-}$ has been reported, and $(ASN)_3[Co(mnt)_3]$ ($\mathbf{3}[ASN]_3$) was prepared by an adaptation of the literature procedure (28% yield).[45]

Crystals suitable for X-ray diffraction were grown by slow evaporation of concentrated acetone/2-propanol solutions. The solid-state structure of $\mathbf{1}[ASN]_3$ reveals a slightly distorted octahedral IrS_6 inner coordination sphere with an average Ir−S distance of 2.348(4) Å (Figure 1a). The structure of $\mathbf{2}[ASN]_3$ is similar to that of $\mathbf{1}[ASN]_3$, with an average Rh−S distance of 2.342(7) Å (Supporting Information, Figure S3). This contrasts with the structure of $\mathbf{3}[ASN]_3$, whose average Co−S distance is 2.259(4) Å (Supporting Information, Figure S4).

Cyclic Voltammetry and Redox Activity of $\mathbf{1}[ASN]_3$. The cyclic voltammetry of $\mathbf{1}[ASN]_3$ shows two reversible oxidation waves at −0.30 and 0.36 V versus $Fc^{+/0}$ (Figure 2a). An additional, irreversible oxidation occurs at 0.88 V. UV−vis spectroelectrochemistry measured at potentials between −0.50 and 0.90 V shows two sets of isosbestic points, suggesting the accessibility of two stable, higher-valent species, presumably $[Ir(mnt)_3]^{2-}$ and $[Ir(mnt)_3]^{-}$ (Figure 2b). Isosbestic points are not encountered in spectral changes beyond 0.6 V, indicating decomposition at these high potentials. Chemical oxidation of $\mathbf{1}[ASN]_3$ with 1 equiv of $FcPF_6$ in dichloromethane affords a green solution. Diffusion of diethyl ether into this solution gave dark red needles of $(ASN)_4[Ir(mnt)_3]_2$ ($\{\mathbf{4}[ASN]_2\}_2$) in quantitative yield (Scheme 2). X-ray structural analysis of $\{\mathbf{4}[ASN]_2\}_2$ reveals a remarkable structure that features two closely packed $[Ir(mnt)_3]^{2-}$ complex ions (Figure 1b). The mutual orientation of the olefin backbones of proximal mnt ligands precludes π-stacking as a driving force for this intermolecular association. However, a significant interaction between the two complexes can be inferred by the short intermolecular S···S separations at 2.741(3) and 3.050(3) Å.

This prediction is borne out by SQUID magnetometry, which shows strong antiferromagnetic coupling between these formally $S = {}^1/_2$ complex ions (Figure 3). The strength of this coupling is too high to permit a precise estimation of J values from the magnetometry data. The SQUID data for $\{\mathbf{4}[ASN]_2\}_2$ show a large amount of temperature-independent paramagnetism contribution (TIP, $\chi_{TIP} = 1.11 \times 10^{-3}$ cm^3 mol^{-1}). This TIP behavior has been described previously for a series of Re(II) complexes for which χ_{TIP} was in the range of $(1.36-1.79) \times 10^{-3}$ cm^3 mol^{-1}.[46] Through experimental and theoretical studies, Dunbar and co-workers established that the large TIP contribution observed for these $S = 1/2$ complexes resulted from strong spin−orbit coupling ($\lambda = 2000-3000$ cm^{-1}), by virtue of the presence of a 5d metal center.[47,48] Other Re(II) complexes supported by redox-active tetrathiafulvalene phosphine ligands exhibited even larger TIP contributions, with χ_{TIP} values in the range of $(9.34-10.7) \times 10^{-3}$ cm^3 mol^{-1}.[49]

In contrast to $\mathbf{1}[ASN]_3$, oxidation of the PPh_4^+ analogue $\mathbf{1}[PPh_4]_3$ produces a green solution from which may be crystallized green needles of monomeric $\mathbf{4}[PPh_4]_2$ (Scheme 2 and Supporting Information, Figure S6). SQUID magnetometry is consistent with an $S = {}^1/_2$ ground state for this species, although it too exhibits a large TIP (Figure 3, $\chi_{TIP} = 3.82 \times 10^{-3}$ cm^3 mol^{-1}). Field-dependent SQUID data (Supporting Information, Figure S1) were measured to exclude the presence of ordering paramagnetic impurities as an origin for the anomalously high $\chi_M T$ values. The solution vis−NIR spectrum of $\{\mathbf{4}[ASN]_2\}_2$ shows remarkable similarity to the solid-state spectrum of $\mathbf{4}[PPh_4]_2$ while bearing no resemblance to its own solid-state spectrum (Figure 4a). This spectroscopic evidence of $\{\mathbf{4}[ASN]_2\}_2$ dissociation in solution is further supported by time-dependent DFT (TDDFT) calculations, which reproduce with good fidelity the dramatic differences between monomeric and dimeric $[Ir(mnt)_3]^{2-}$ in the near-infrared (NIR) region (Figure 4b).

Chemical oxidation of $\mathbf{1}[ASN]_3$ with 2 equiv of tris(4-bromophenyl)aminium hexachloroantimonate ("magic blue") presumably generates $[Ir(mnt)_3]^{-}$, although analytically pure material was not isolated. Extended X-ray absorption fine structure (EXAFS) analysis of the reaction mixture shows that the orange oxidation product retains the tris(mnt) coordination sphere, with average bond metrics in reasonable agreement

DOI: 10.1021/acs.inorgchem.5b00289
Inorg. Chem. 2015, 54, 3660−3669

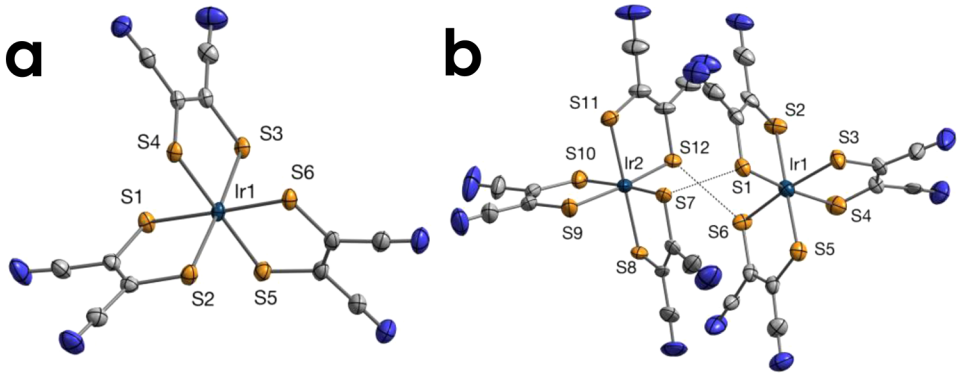

Figure 1. (a) Thermal ellipsoid plot of the complex anion in crystals of $\mathbf{1}[ASN]_3$. The complex is very close to ideal octahedral geometry, and the average Ir−S distance is 2.348(4) Å. ASN counterions were omitted for clarity. Thermal ellipsoids are plotted at 50% probability. (b) Thermal ellipsoid plot of the dimeric complex anion in crystals of $\{\mathbf{4}[ASN]_2\}_2$ at 50% probability. The structure reveals close S···S distances between the two complex ions of 2.741(3) and 3.050(3) Å.

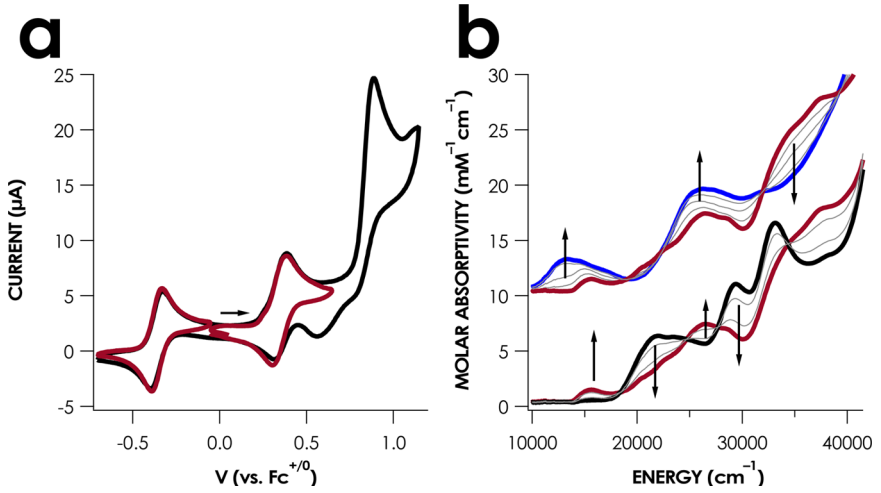

Figure 2. (a) CV of $\mathbf{1}[ASN]_3$ measured from −0.70 to 1.20 V (vs $Fc^{+/0}$) in MeCN with 0.1 M $[(nBu)_4N]PF_6$ (100 mV/s). The first and second oxidations to $[Ir(mnt)_3]^{2-}$ and $[Ir(mnt)_3]^{-}$ are reversible; isolated voltammograms are superimposed in red. (b) UV−vis spectra measured at discrete reduction potentials from −0.50 to 0.90 V vs $Fc^{+/0}$ show isosbestic points consistent with clean formation of two new species. The UV−vis spectrum of $\mathbf{1}[ASN]_3$ is black, and the spectrum of $\{\mathbf{4}[ASN]_2\}_2$ is red. The blue trace is assigned to the putative $[Ir(mnt)_3]^{-}$ species.

Scheme 2. Chemical Oxidation of $\mathbf{1}[cat]_3$ (cat = ASN, PPh_4) Results in the Formation of Dimeric $\{\mathbf{4}[ASN]_2\}_2$ and Monomeric $\mathbf{4}[PPh_4]_2$

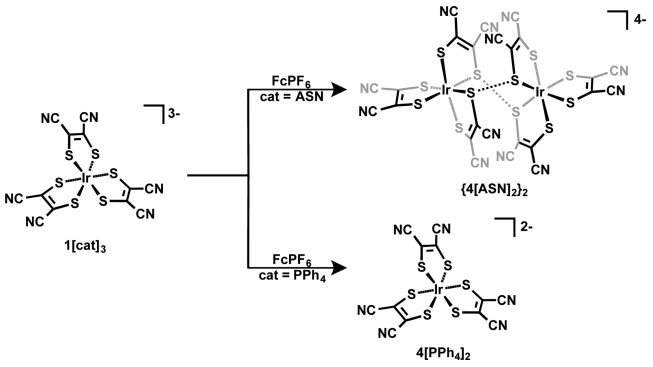

with a DFT-calculated structure of $[Ir(mnt)_3]^{-}$ (Supporting Information, Figure S19 and Table S13). Further characterization was not pursued.

Probing the Nature of the S···S Interaction in $\{\mathbf{4}[ASN]_2\}_2$. The close proximity of the two complexes in

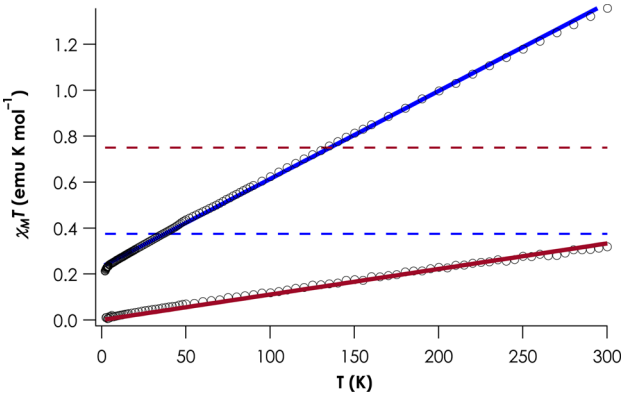

Figure 3. Plot of χT vs T from SQUID magnetometry of powdered $\{\mathbf{4}[ASN]_2\}_2$ (red) and $\mathbf{4}[PPh_4]_2$ (blue). The data are open circles; fits to the data are solid lines. Dashed lines are shown to indicate idealized g = 2.0 spin-only values for the triplet expected for a hypothetically uncoupled complex ion dimer in $\{\mathbf{4}[ASN]_2\}_2$ and for the doublet state of the monomeric complex ion in $\mathbf{4}[PPh_4]_2$. Fitting parameters: $\{\mathbf{4}[ASN]_2\}_2$: $\chi_{TIP} = 1.11 \times 10^{-3}$ cm^3 mol^{-1}; $\mathbf{4}[PPh_4]_2$: g = 1.572(4), $\chi_{TIP} = 3.82 \times 10^{-3}$ cm^3 mol^{-1}.

DOI: 10.1021/acs.inorgchem.5b00289
Inorg. Chem. 2015, 54, 3660−3669

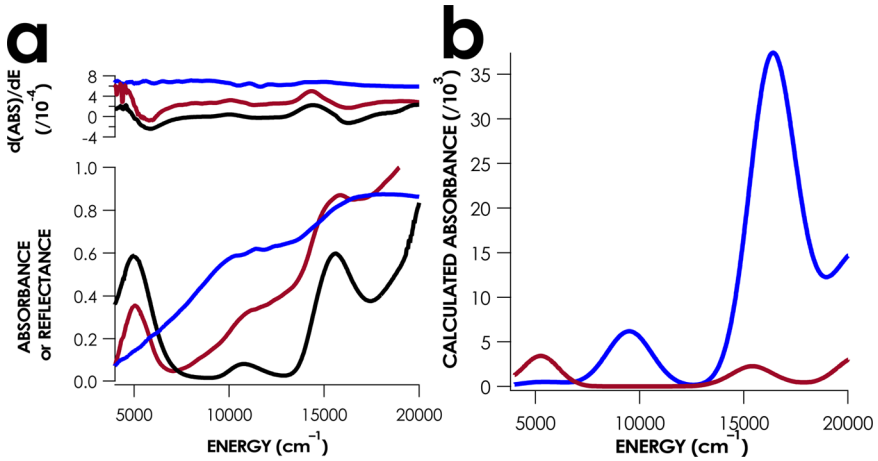

Figure 4. (a) vis−NIR spectra and their first derivatives with respect to energy measured by transmission either through solution or through powder pressed between sapphire plates for $\{4[ASN]_2\}_2$ in MeCN solution (black), powdered $\{4[ASN]_2\}_2$ (blue), and powdered $4[PPh_4]_2$ (red). (b) TDDFT (B3LYP-def2-TZVP-ZORA) calculated vis−NIR spectra for monomeric $[Ir(mnt)_3]^{2-}$ (red) and $[Ir(mnt)_3]_2^{4-}$ (blue).

dimeric $\{4[ASN]_2\}_2$ is puzzling owing to the charge of each $[Ir(mnt)_3]^{2-}$ unit. The 2.741(3) and 3.050(3) Å S···S distances suggest that these Ir-bound $mnt^{\bullet-}$ S atoms are coupled, either via covalent bonding or diradical bonding. These possibilities were explored through broken symmetry (BS[57]) DFT and ab initio SORCI[42] calculations. No BS solution emerges, suggesting that the $\{4[ASN]_2\}_2$ dimer associates via a bona fide covalent S−S bond rather than through a diradical bond.[10,58] Our SORCI results support this interpretation of the S−S interaction: the dominant (82%) ground-state electronic configuration of the $\{4[ASN]_2\}_2$ dimer features a doubly occupied S−S σ-bonding orbital (Figure 5a). The S···S

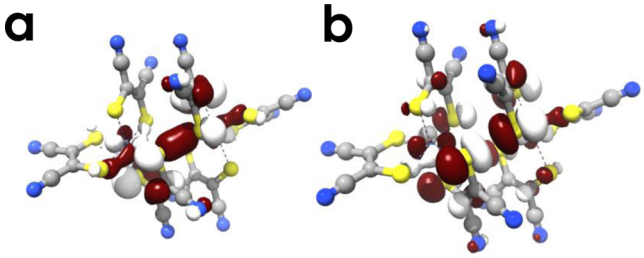

Figure 5. Averaged atomic natural orbital plots of the (a) HOMO and (b) LUMO of dimeric $\{4[ASN]_2\}_2$. The HOMO is predominantly of S−S σ-bonding character, while the LUMO is dominated by the corresponding S−S σ-antibonding interaction. Orbitals are plotted at an isolevel of 0.3 e $Å^{-3}$.

distances in $\{4[ASN]_2\}_2$ suggest that the S−S covalent bond is substantially weaker than in typical disulfides, which have S···S distances on the order of 2.02−2.04 Å.[59,60]

Excited-state calculations were used to estimate the strength of the shorter S−S bond in $\{4[ASN]_2\}_2$. In the four-state paradigm for a covalent bond proposed by Coulson and Fischer,[61] bond energy is taken as the energetic separation between the singlet state arising from full occupation of the bonding molecular orbital (MO) and the triplet state arising from single occupation of the bonding and antibonding MOs by electrons with parallel spins. Our SORCI calculations indicate that the dominant (79%) electronic configuration of the first triplet excited state in $\{4[ASN]_2\}_2$ has an electronic configuration in which the S−S σ and σ^* orbitals are singly occupied (Figure 5b). This state is calculated to be to 4100 cm^{-1} higher energy relative to the ground state and implies a bond energy of ca. 12 kcal mol^{-1}. A similar SORCI calculation of the $[(mnt)_2]^{2-}$ dimer, whose structure is provided in the Supporting Information (Figure S9), gives an S−S bond energy of 36.0 kcal mol^{-1}. The smaller S−S bond energy of the $\{4[ASN]_2\}_2$ dimer accords with Ir 5d dilution of the S 3p character in the interacting orbitals. A similar rationale may be used for the smaller bond energy of mnt_2^{2-} relative to that of Me_2S_2 (62.0 kcal mol^{-1}),[62] which reflects the dilution of S 3p character in the frontier orbitals by admixture with the C orbitals of the conjugated mnt backbone.

Cyclic Voltammetry and Redox Activity of $2[ASN]_3$ and $3[ASN]_3$. The cyclic voltammogram of $3[ASN]_3$ is devoid of reversible oxidations up to scan rates of 1 V/s at 298 K, suggesting that $[Co(mnt)_3]^{2-}$ decomposes on the electrochemical time scale (Supporting Information, Figure S12a). However, UV−vis spectroelectrochemistry measured between −0.50 and 1.00 V versus $Fc^{+/0}$ indicates conversion to at least two new species (Supporting Information, Figures S14 and S15). Chemical oxidation with stoichiometric $FcPF_6$ yields the dimeric complex $(ASN)_2[Co(mnt)_2]_2$ ($\{6[ASN]\}_2$) in 77% yield (Scheme 3, Figure 6a). This structural motif is well-known.[50,51] High-resolution ESI-MS of the reaction mixture suggests that "$mnt^{\bullet-}$" is formed as a byproduct (Supporting Information, Figure S11). We cannot rule out formation of

Scheme 3. Chemical Oxidation of $2[ASN]_3$ and $3[ASN]_3$ Generates Homobimetallic $5[ASN]_4$ and Dimeric $\{6[ASN]\}_2$

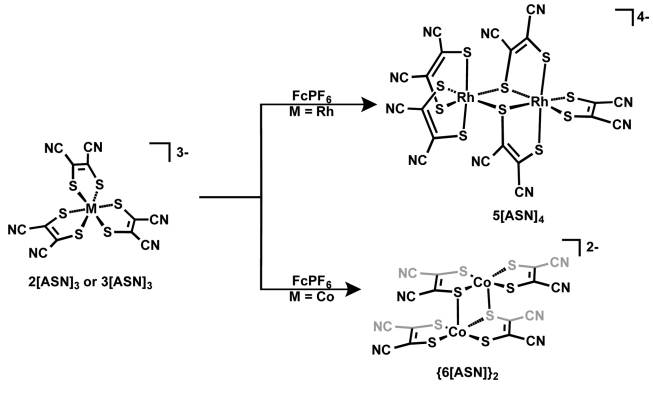

DOI: 10.1021/acs.inorgchem.5b00289
Inorg. Chem. 2015, 54, 3660−3669

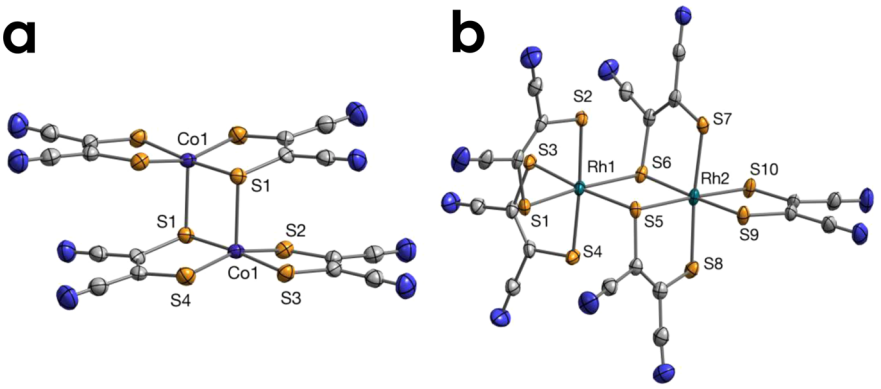

Figure 6. (a) Thermal ellipsoid plot of the complex anion in $\{\mathbf{6}[ASN]\}_2$ at 50% probability level. (b) Thermal ellipsoid plot of the complex anion in $\mathbf{5}[ASN]_4$ at 50% probability level. The complex has an unusual geometry best described as a $[Rh(mnt)_2]^-$ moiety coordinating to a $[Rh(mnt)_3]^{3-}$ moiety with the average nonbridging Rh−S distance being 2.336(9) Å. The Rh−S distances involving bridging S atoms are Rh1−S5: 2.431(1) Å, Rh1−S6: 2.432(1) Å, Rh2−S5: 2.355(1) Å, and Rh2−S6: 2.363(1) Å. Counterions were omitted for clarity in both (a) and (b).

mnt_2^{2-}, which we found to fragment under our conditions for ESI-MS. Spectroelectrochemical data collected via oxidation of $\mathbf{3}[ASN]_3$ show features characteristic of $\{\mathbf{6}[ASN]\}_2$; however, these data also indicate that additional, unidentified species are formed electrochemically.

The cyclic voltammetry of $\mathbf{2}[ASN]_3$ exhibits quasi-reversible oxidations at −0.04 and 0.39 V versus $Fc^{+/0}$ (Supporting Information, Figure S12b). However, treatment of $\mathbf{2}[ASN]_3$ with 1 equiv of $FcPF_6$ does not result in the formation of $(ASN)_2[Rh(mnt)_3]$. Rather, the homobimetallic Rh^{III} compound $(ASN)_4[Rh_2(mnt)_5]$ ($\mathbf{5}[ASN]_4$) is isolated in 45% yield (Scheme 3, Figure 6b). A similar yield is achieved using 0.5 equiv of $FcPF_6$.

The dinuclear complex ion in $\mathbf{5}[ASN]_4$ is not a dimer but rather forms by filling the octahedral coordination sphere of a $[Rh(mnt)_2]^-$ unit with bridging thiolates donated from an intact $[Rh(mnt)_3]^{3-}$. This molecule presumably forms via dissociation of $mnt^{\bullet-}$ (Supporting Information, Figure S11) from one Rh center, after which the coordination sphere is filled via bridging S-ligation from an intact $[Rh(mnt)_3]^{3-}$. We note that this edge-sharing bioctahedral motif is rare—related species include Re and Mo tris(dithiolenes) as well as Co and Ru tris(dithiocarbamates).[52−56] In these cases, the coordination spheres are distorted from octahedral geometry, and the metrical parameters show evidence of metal−metal interactions. In $\mathbf{5}[ASN]_4$ however, the octahedra are unperturbed, and the Rh···Rh distance of 3.5759(4) Å is inconsistent with a metal−metal interaction. Formation of $\mathbf{5}[ASN]_4$ is rapid, as evidenced by the appearance of a feature at 0.28 V versus $Fc^{+/0}$ in the cyclic voltammogram of $\mathbf{3}[ASN]_3$, corresponding to the $[Rh_2(mnt)_5]^{2-/3-}$ couple (Supporting Information, Figures S12b and S13). Similar to $\{\mathbf{6}[ASN]\}_2$, electrochemical generation of $\mathbf{5}[ASN]_4$ does not proceed cleanly as shown by comparison of spectroelectrochemical data of the UV−vis spectrum of the pure compound (Supporting Information, Figures S16 and S17).

Electronic Structures of Dianionic Group 9 Tris(dithiolenes). To rationalize the one-electron reactivity of group 9 tris(mnt) complexes (summarized in Schemes 2 and 3), we used DFT to calculate ground-state electronic structures for the hypothetical dianionic tris(mnt) monomers. Quasi-restricted orbital (QRO) transformations[63] of calculations at the B3LYP/def2-TZVP-ZORA level[34,39] show that the singly occupied molecular orbital (SOMO) of the Co congener is wholly S-centered and is isotropically distributed over the six S atoms in the molecule in an orbital of A_2 symmetry (D_3) that is unable to mix with the E and A_1 symmetry d-orbitals. In contrast, the Rh and Ir congeners have E symmetry SOMOs with 17% and 26% metal character, respectively (Figure 7). The

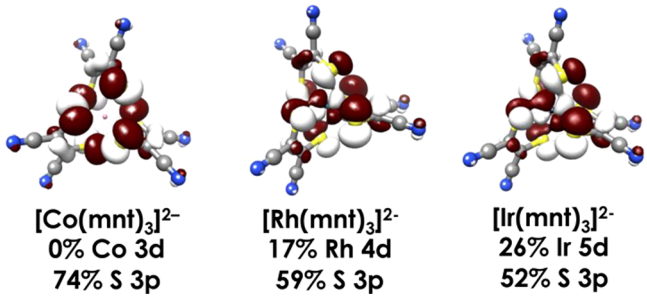

Figure 7. QRO plots of the SOMOs of $[M(mnt)_3]^{2-}$ (M = Co, Rh, Ir). QROs were calculated at the B3LYP/def2-TZVP-ZORA level. Orbitals are plotted at an isosurface level of 0.3 e $Å^{-3}$.

remaining SOMO character in the Rh and Ir complexes is of S 3p parentage, although in both cases the S 3p orbital coefficients of one mnt ligand are twofold larger than in the other two mnt ligands (Supporting Information, Table S14). The observation of nonequivalent S−S distances (2.741(3) and 3.050(3) Å) in $\{\mathbf{4}[ASN]_2\}_2$ accords with this anisotropic distribution of S character calculated in the radical SOMO of each $[Ir(mnt)_3]^{2-}$ unit. Moreover, the structure of $\mathbf{4}[PPh_4]_2$ shows evidence of a static Jahn−Teller distortion consistent with the ^2E ground state calculated for $[Ir(mnt)_3]^{2-}$.[64] The Ir−S distances for two mnt ligands are 2.340 Å, while the Ir−S distances for the disordered third mnt are 2.277(4) and 2.184(7) Å. Moreover, modest Jahn−Teller splitting of the SOMO is consistent with the large TIP exhibited by both $\{\mathbf{4}[ASN]_2\}_2$ and $\mathbf{4}[PPh_4]_2$, as well as the inability to observe their EPR spectra at temperatures greater than or equal to 10 K.[65,66]

For $[Ir(mnt)_3]^{2-}$, the radical hole has greater metal character than in the Co and Rh congeners. This suggests that the $mnt^{\bullet-}$ units retain sufficient donor strength to disfavor dissociation. Because $\{\mathbf{4}[ASN]_2\}_2$ gave no EPR signal, the relative Ir and S contributions to the SOMO of this species was examined using XAS. Ir L_1-edge XAS probes core-to-valence excitations from the 2s subshell. The first inflection points of *ns*-to-valence XAS

DOI: 10.1021/acs.inorgchem.5b00289
Inorg. Chem. 2015, 54, 3660−3669

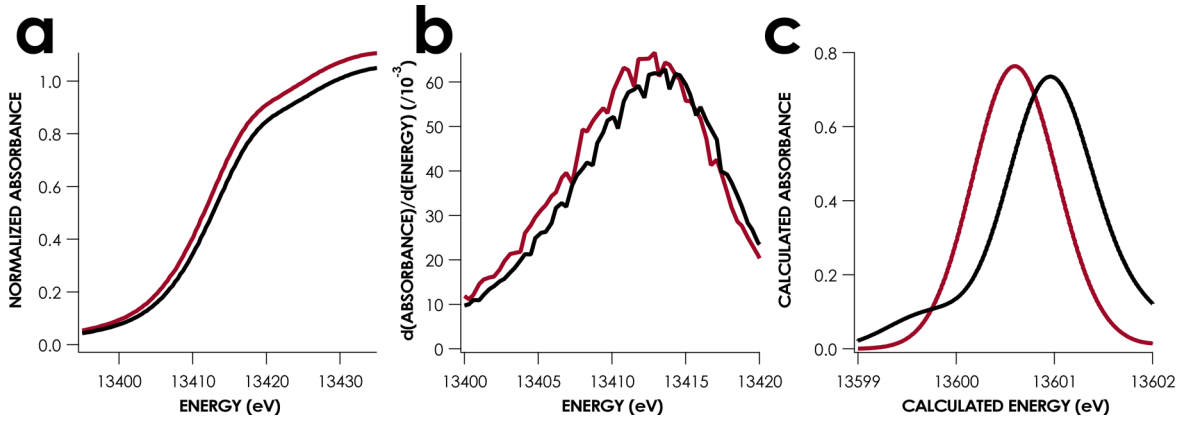

Figure 8. (a) Experimental, (b) zoomed first-derivative, and (c) TDDFT-calculated (B3LYP-def2-TZVP-ZORA) Ir L_1-edge XAS spectra for **1**[ASN]$_3$ (black) and {**4**[ASN]$_2$}$_2$ (red). In the calculated spectra, the energy axis has not been adjusted to correct for inaccuracy in modeling the Ir 2s binding energy.

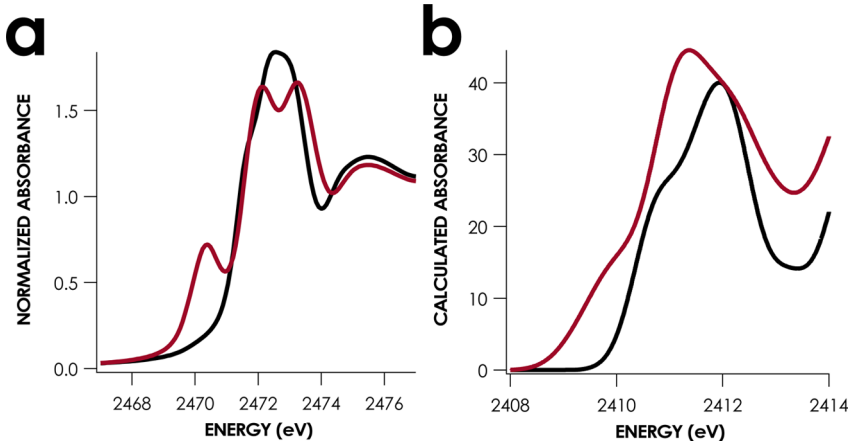

Figure 9. (a) S K-edge XAS of solid **1**[ASN]$_3$ (black) and {**4**[ASN]$_2$}$_2$ (red). The pre-edge feature in the spectrum of {**4**[ASN]$_2$}$_2$ is diagnostic of an orbital vacancy with significant S-character. This assignment is verified by the TDDFT-calculated (B3LYP-def2-TZVP-ZORA) S K-edge XAS spectra shown in (b). The energy axis of the calculated spectra has not been corrected for inaccuracy in modeling the S 1s binding energy.

spectra are typically used as measurements of physical oxidation state.[67,68] For {**4**[ASN]$_2$}$_2$, this occurs 0.7 eV lower in energy than for **1**[ASN]$_3$ (Figure 8a). While this shift in the L_1-edge accords with metal-centered redox, it also implies that {**4**[ASN]$_2$}$_2$ has a *lower* oxidation state than that of **1**[ASN]$_3$. However, the presence of an additional metal-centered orbital vacancy in {**4**[ASN]$_2$}$_2$ will give rise to an Ir 2s → {α(Ir 5d) + [$\sqrt{(1-\alpha^2)}$](S 3p)} pre-edge excitation. This prediction is supported by TDDFT calculations (Figure 8b).[69] Because of the excessive core-hole lifetime broadening endemic to XAS of heavier elements,[70,71] this excitation will be unresolved from the rising edge. Consequently, its presence gives the appearance of an edge shift to lower energy, despite the fact that the metal has been partially oxidized.

The S K-edge XAS of **1**[ASN]$_3$ and {**4**[ASN]$_2$}$_2$ were recorded to probe the S parentage in the SOMO. Pre-edge features observed in S K-edge XAS may be assigned as S 1s → {α(S 3d) + [$\sqrt{(1-\alpha^2)}$](M *n*d)} transitions. The intensities of these transitions thus afford a metric of the S character of MOs proximal to the ligand field. The S K-edge XAS measurements at first glance appear at odds with the covalent bond formalism for the interaction between complex ions in the {**4**[ASN]$_2$}$_2$ dimer. Pre-edge features near 2470 eV are diagnostic of ligand-centered radical character in tris(dithiolene) complexes.[9] Such a feature is visible in the S K-edge XAS spectrum of {**4**[ASN]$_2$}$_2$ (Figure 9a). However, it must be remembered that while the "ligand radical" S−S σ-bonding MO is filled, two holes with equal S-parentage remain in the S−S σ* MO, giving rise to the observed 1s → mnt$^{\bullet-}$ transition in the S K-edge spectrum. This assignment is supported by TDDFT (Figure 9b). Estimation of S parentage per radical hole by the method of Sproules gives a value of 50%,[72] in excellent agreement with the DFT-derived value of 52%.

CONCLUSIONS

Although its lighter congeners decompose following oxidation, **1**[ASN]$_3$ and **1**[PPh$_4$]$_3$ may be cleanly oxidized by a single electron to yield dimeric {**4**[ASN]$_2$}$_2$ and monomeric **4**[PPh$_4$]$_2$, respectively. Spectroelectrochemistry and EXAFS suggest that the complex dianion [Ir(mnt)$_3$]$^{2-}$ may be further oxidized to [Ir(mnt)$_3$]$^-$. Experimentally calibrated DFT calculations imply that the Co congener is unstable following oxidation because an electron is removed from a purely ligand-centered, A_2 symmetry MO, which weakens donor strength sufficient to favor dissociation. The HOMOs of the formally Rh(III) and Ir(III) complexes are of E symmetry, permitting admixture of M 4d/5d character. The greater M−S covalency of the Ir species relative to the Rh congener disfavors dissociation.

DOI: 10.1021/acs.inorgchem.5b00289
Inorg. Chem. 2015, 54, 3660−3669

While the electronic structure of metallodithiolenes is certainly well-trodden ground,[1] our present comparison of the *reactivity* (or lack thereof) following oxidation of group 9 tris(mnt) complexes has implications that should be considered in the design of new transition metal catalysts. For example, multiple catalysts have been reported that exploit metal−ligand cooperativity such that generation of bound ligand radicals permits bond formation with substrate molecules. This type of cooperativity has been used for entantioselective transformations. Zhang and co-workers have reported highly asymmetric cyclopropanation and amination reactions facilitated by cooperativity between Co and bound radicals through the use of chemo- or regioselective supporting ligands.[73,74] Success with this strategy requires bond formation to occur while the radical ligand remains bound to the metal and, consequently, under the influence of the supporting ligand. Work from de Bruin and co-workers has shown that lability of the radical ligand on Co can interfere with such synthetic schemes, with bond-formation occurring after the ligand radical has dissociated from the metal.[75,76] In such cases, enantioinduction fails. The substitution of a late third-row metal in such systems should facilitate retention of the bound radical. Such an approach has precedent in other work from de Bruin, notably in the report of stable Ir-carbene and Ir-nitrene radical species.[77] This principle will guide subsequent work from our laboratory exploiting motifs of modern coordination chemistry, such as second-sphere interactions and redox-noninnocence, for the application of molecular redox processes in catalysis.

■ ASSOCIATED CONTENT

Supporting Information

Details of physical measurements, including SQUID magnetometry, infrared data, mass spectrometry data, calculations, and crystallographic data. CCDC: 1031447, 1009417−1009423. This material is available free of charge via the Internet at http://pubs.acs.org.

■ AUTHOR INFORMATION

Corresponding Author

*E-mail: kml236@cornell.edu.

Notes

The authors declare no competing financial interest.

■ ACKNOWLEDGMENTS

K.M.L. gratefully acknowledges the Cornell University College of Arts and Sciences for startup funding. T.J.M. thanks the Oticon Foundation and Knud Højgaards Foundation for travel grants in support of this work. J.B. acknowledges support from the Danish Research Councils for Independent Research (12-125226). J.W.H.U. is an NSF Graduate Research Fellow (DGE-1144153). This work is based in part upon research conducted at the Stanford Synchrotron Radiation Lightsource. Use of the Stanford Synchrotron Radiation Lightsource, SLAC National Accelerator Laboratory, is supported by the U.S. Department of Energy (DOE), Office of Science, Office of Basic Energy Sciences under Contract No. DE-AC02-76SF00515. The SSRL Structural Molecular Biology Program is supported by the DOE Office of Biological and Environmental Research and by the National Institutes of Health, National Institute of General Medical Sciences (including P41GM103393).

■ REFERENCES

(1) Sproules, S. *Prog. Inorg. Chem.* **2014**, *58*, 1−144.
(2) Eisenberg, R. *Coord. Chem. Rev.* **2011**, *255*, 825−836.
(3) Eisenberg, R.; Gray, H. B. *Inorg. Chem.* **2011**, *50*, 9741−9751.
(4) *Inorg. Chem.* **2011**, *50*, 9737−9914.
(5) Eur, J. *Inorg. Chem.* **2012**, *3*, 340−580.
(6) Luca, O. R.; Crabtree, R. H. *Chem. Soc. Rev.* **2013**, *42*, 1440−1459.
(7) Lyaskovskyy, V.; de Bruin, B. *ACS Catal.* **2012**, *2*, 270−279.
(8) Suarez, A. I. O.; Lyaskovskyy, V.; Reek, J. N.; van der Vlugt, J. I.; de Bruin, B. *Angew. Chem., Int. Ed.* **2013**, *52*, 12510−12529.
(9) Sproules, S.; Wieghardt, K. *Coord. Chem. Rev.* **2011**, *255*, 837−860.
(10) Tomson, N. C.; Crimmin, M. R.; Petrenko, T.; Rosebrugh, L. E.; Sproules, S.; Boyd, W. C.; Bergman, R. G.; DeBeer, S.; Toste, F. D.; Wieghardt, K. *J. Am. Chem. Soc.* **2011**, *133*, 18785−18801.
(11) Tenderholt, A. L.; Szilagyi, R. K.; Holm, R. H.; Hodgson, K. O.; Hedman, B.; Solomon, E. I. *J. Inorg. Biochem.* **2007**, *101*, 1594−1600.
(12) Ray, K.; DeBeer George, S.; Solomon, E. I.; Wieghardt, K.; Neese, F. *Chem.—Eur. J.* **2007**, *13*, 2783−2797.
(13) Tsujimoto, Y.; Tassel, C.; Hayashi, N.; Watanabe, T.; Kageyama, H.; Yoshimura, K.; Takano, M.; Ceretti, M.; Ritter, C.; Paulus, W. *Nature* **2007**, *450*, 1062−1065.
(14) Bart, S. C.; Chlopek, K.; Bill, E.; Bouwkamp, M. W.; Lobkovsky, E.; Neese, F.; Wieghardt, K.; Chirik, P. J. *J. Am. Chem. Soc.* **2006**, *128*, 13901−13912.
(15) Knijnenburg, Q.; Gambarotta, S.; Budzelaar, P. H. *Dalton Trans.* **2006**, 5442−5448.
(16) Heyduk, A. F.; Zarkesh, R. A.; Nguyen, A. I. *Inorg. Chem.* **2011**, *50*, 9849−9863.
(17) Palmer, J. H.; Lancaster, K. M. *Inorg. Chem.* **2012**, *51*, 12473−12482.
(18) Almlöfl, J.; Gropen, O. *Rev. Comput. Chem.* **2009**, *8*, 203.
(19) Pyykkö, P. *Chem. Rev.* **1988**, *88*, 563−594.
(20) Autschbach, J. *J. Chem. Phys.* **2012**, *136*, 150902.
(21) Pyykkö, P. *Annu. Rev. Phys. Chem.* **2012**, *63*, 45−64.
(22) Werden, B. G.; Billig, E.; Gray, H. B. *Inorg. Chem.* **1966**, *5*, 78−81.
(23) Aitken, R. A.; Philp, E. F.; Riddell, F. G.; Smith, M. H. *ARKIVOC* **2002**, *3*, 63−70.
(24) Davison, A.; Holm, R.; Benson, R.; Mahler, W. *Inorg. Synth.* **2007**, *10*, 8−26.
(25) Bruker; Bruker AXS, Inc. *SAINT,* Version 7.68A; Bruker AXS: Madison, WI, 2009.
(26) Sheldrick, G.; *SADABS,* Version 2008/2; University of Göttingen: Germany, 2003.
(27) Dolomanov, O. V.; Bourhis, L. J.; Gildea, R. J.; Howard, J. A.; Puschmann, H. *J. Appl. Crystallogr.* **2009**, *42*, 339−341.
(28) Webb, S. *Phys. Scr.* **2005**, *2005*, 1011.
(29) Rehr, J. J.; Albers, R. *Rev. Mod. Phys.* **2000**, *72*, 621.
(30) Rehr, J. J.; Kas, J. J.; Prange, M. P.; Sorini, A. P.; Takimoto, Y.; Vila, F. *C. R. Phys.* **2009**, *10*, 548−559.
(31) Neese, F. *ORCA,* an ab initio, Density Functional and Semiempirical program package, Version 2.9.0; Max-Planck-Insitut für Bioanorganische Chemie: Mülheim and der Ruhr, 2004.
(32) Becke, A. D. *Phys. Rev. A* **1988**, *38*, 3098−3100.
(33) Perdew, J. P. *Phys. Rev. B: Condens. Matter* **1986**, *33*, 8822−8824.
(34) Pantazis, D. A.; Chen, X.-Y.; Landis, C. R.; Neese, F. *J. Chem. Theory Comput.* **2008**, *4*, 908−919.
(35) Weigend, F.; Ahlrichs, R. *Phys. Chem. Chem. Phys.* **2005**, *7*, 3297−3305.
(36) van Lenthe, E.; van der Avoird, A.; Wormer, P. E. S. *J. Chem. Phys.* **1998**, *108*, 4783−4796.
(37) van Wüllen, C. *J. Chem. Phys.* **1998**, 109.
(38) Klamt, A.; Schuurmann, G. *J. Chem. Soc., Perkin Trans. 2* **1993**, *2*, 799−805.
(39) Stephens, P.; Devlin, F.; Chabalowski, C.; Frisch, M. J. *J. Phys. Chem.* **1994**, *98*, 11623−11627.

DOI: 10.1021/acs.inorgchem.5b00289
Inorg. Chem. 2015, 54, 3660−3669

(40) Neese, F. *J. Chem. Phys.* **2001**, *115*, 11080−11096.
(41) Neese, F. *J. Chem. Phys.* **2005**, *122*, 034107.
(42) Neese, F. *J. Chem. Phys.* **2003**, *119*, 9428−9443.
(43) McCleverty, J. A. *Prog. Inorg. Chem.* **1968**, *10*, 49−221.
(44) Burns, R.; McAuliffe, C. *Adv. Inorg. Chem. Radiochem.* **1979**, *22*, 303−348.
(45) McCleverty, J.; Locke, J.; Wharton, E.; Gerloch, M. *J. Chem. Soc. A* **1968**, 816−823.
(46) Schelter, E. J.; Jitendra, K. B.; Galán-Mascarós, J. R.; Dunbar, K. R. *Inorg. Chem.* **2003**, *42*, 4256−4258.
(47) Dunbar, K. R.; Schelter, E. J.; Tsukerblat, B. S.; Ostrovsky, S. M.; Mirovitsky, V. Y.; Palii, A. V. *Polyhedron* **2003**, *22*, 2545−2556.
(48) Dunbar, K. R.; Schelter, E. J.; Palii, A. V.; Ostrovsky, S. M.; Mirovitsky, V. Y.; Hudson, J. M.; Omary, M. A.; Klokishner, S. I.; Tsukerblat, B. S. *J. Phys. Chem. A* **2003**, *107*, 11102−11111.
(49) Uzelmeier, C. E.; Bartley, S. L.; Fourmigué, M.; Rogers, R.; Grandinetti, G.; Dunbar, K. R. *Inorg. Chem.* **1998**, *37*, 6706−6713.
(50) Balch, A. L.; Dance, I. G.; Holm, R. H. *J. Am. Chem. Soc.* **1968**, *90*, 1139−1145.
(51) McNamara, W. R.; Han, Z.; Yin, C.-J. M.; Brennessel, W. W.; Holland, P. L.; Eisenberg, R. *Proc. Natl. Acad. Sci. U. S. A.* **2012**, *109*, 15594−15599.
(52) Hendrickson, A.; Martin, R.; Taylor, D. *Aust. J. Chem.* **1976**, *29*, 269−273.
(53) Raston, C. L.; White, A. H. *J. Chem. Soc., Dalton Trans.* **1975**, 2410−2418.
(54) Halbert, T. R.; Stiefel, E. I. *Inorg. Chem.* **1989**, *28*, 2501−2503.
(55) Matsubayashi, G.; Maikawa, T.; Tamura, H.; Nakano, M.; Arakawa, R. *J. Chem. Soc., Dalton Trans.* **1996**, 1539−1544.
(56) Yan, Y.; Mague, J. T.; Donahue, J. P.; Sproules, S. *Chem. Commun.* **2015**, DOI: 10.1039/c4cc09397f.
(57) Noodleman, L. *J. Chem. Phys.* **1981**, *74*, 5737−5743.
(58) Brown, C. A.; Pavlosky, M. A.; Westre, T. E.; Zhang, Y.; Hedman, B.; Hodgson, K. O.; Solomon, E. I. *J. Am. Chem. Soc.* **1995**, *117*, 715−732.
(59) Sutter, D.; Dreizler, H.; Rudolf, H. D. *Z. Naturforsch., A: Phys. Sci.* **1965**, *20*, 1676.
(60) Beagley, B.; McAloon, K. T. *Trans. Faraday. Soc.* **1971**, *67*, 1676.
(61) Coulson, C. A.; Fischer, I. *Philos. Mag.* **1949**, *40*, 386−393.
(62) Jursic, B. S. *Int. J. Quantum Chem.* **1997**, *62*, 291−296.
(63) Neese, F. *J. Am. Chem. Soc.* **2006**, *128*, 10213−10222.
(64) Jahn, H. A.; Teller, E. *Proc. R. Soc. London, Ser. A* **1937**, 220−235.
(65) Bates, C. A. *Phys. Rep.* **1978**, *35*, 187−304.
(66) Krebs, J.; Stauss, G. *Phys. Rev. B: Condens. Matter* **1977**, *15*, 17.
(67) De Groot, F. *Chem. Rev.* **2001**, *101*, 1779−1808.
(68) Glatzel, P.; Bergmann, U. *Coord. Chem. Rev.* **2005**, *249*, 65−95.
(69) DeBeer George, S.; Petrenko, T.; Neese, F. *J. Phys. Chem. A* **2008**, *112*, 12936−12943.
(70) Krause, M. O.; Oliver, J. *J. Phys. Chem. Ref. Data* **1979**, *8*, 329−338.
(71) Hämäläinen, K.; Siddons, D.; Hastings, J.; Berman, L. *Phys. Rev. Lett.* **1991**, *67*, 2850.
(72) Sproules, S.; Weyhermüller, T.; Goddard, R.; Wieghardt, K. *Inorg. Chem.* **2011**, *50*, 12623−12631.
(73) Xu, X.; Lu, H.; Ruppel, J. V.; Cui, X.; Lopez de Mesa, S.; Wojtas, L.; Zhang, X. P. *J. Am. Chem. Soc.* **2011**, *133*, 15292−15295.
(74) Lu, H.; Hu, Y.; Jiang, H.; Wojtas, L.; Zhang, X. P. *Org. Lett.* **2012**, *14*, 5158−5161.
(75) Paul, N. D.; Chirila, A.; Lu, H.; Zhang, X. P.; de Bruin, B. *Chem.—Eur. J.* **2013**, *19*, 12953−12958.
(76) Paul, N. D.; Mandal, S.; Otte, M.; Cui, X.; Zhang, X. P.; de Bruin, B. *J. Am. Chem. Soc.* **2014**, *136*, 1090−1096.
(77) De Bruin, B.; Hetterscheid, D. G.; Koekkoek, A. J.; Gruetzmacher, H. *Prog. Inorg. Chem.* **2007**, 247−354.

DOI: 10.1021/acs.inorgchem.5b00289
Inorg. Chem. 2015, 54, 3660−3669